arXiv:1410.5542v1 [astro-ph.SR] 21 Oct 2014

INVESTIGATION OF FORCE-FREENESS OF A SOLAR EMERGING MAGNETIC FIELD VIA APPLICATION OF THE VIRIAL THEOREM TO MHD SIMULATIONS

Jihye KANG

School of Space Research, Kyung Hee University, 1, Seocheon-dong, Yongin, 446-701, Korea

siriustar@khu.ac.kr

and

Tetsuya MAGARA

Department of Astronomy and Space Science, School of Space Research, Kyung Hee University, 1, Seocheon-dong, Yongin, 446-701, Republic of Korea

(Received ; accepted)

Abstract

Force-freeness of a solar magnetic field is a key to reconstructing invisible coronal magnetic structure of an emerging flux region on the Sun where active phenomena such as flares and coronal mass ejections frequently occur. We have performed magnetohydrodynamic (MHD) simulations which are adjusted to investigate force-freeness of an emerging magnetic field by using the virial theorem. Our focus is on how the force-free range of an emerging flux region develops and how it depends on the twist of a pre-emerged magnetic field. As an emerging flux region evolves, the upper limit of the force-free range continuously increases while the lower limit is asymptotically reduced to the order of a photospheric pressure scale height above the solar surface. As the twist becomes small the lower limit increases and then seems to be saturated. We also discuss the applicability of the virial theorem to an evolving magnetic structure on the Sun. **A manuscript with high-resolution figures is found at http://web.khu.ac.kr/∼magara/index.html. Here '∼' is a tilde.**

Key words: Sun: magnetic fields — Sun: activity — Sun: corona — magnetohydrodynamics (MHD) — methods: numerical

1. Introduction

Active phenomena such as flares and coronal mass ejections (CMEs) are frequently observed on the Sun and it is now believed that they are caused by the release of free magnetic energy in the solar corona. An emerging flux region with intense magnetic flux in it is a typical area where active

phenomena occurs, which is called an *active region* (Forbes 2000; Shibata & Magara 2011; Chen 2011). In order to understand the physical mechanism for producing active phenomena it is important to know the coronal magnetic structure of an emerging flux region, although it is still difficult to derive a detailed configuration of a coronal magnetic field only by observations. We therefore need to reconstruct a coronal magnetic structure using observable quantities. A photospheric magnetic field is one of these observable quantities and the vector information on a photospheric field has widely been used to reconstruct a magnetic structure with free magnetic energy in the corona (Wang et al. 1994; Cameron & Sammis 1999; Régnier & Amari 2004; Wang 2006).

One of the ways to reconstruct a coronal magnetic structure is to solve the so-called force-free equation given by (e.g. Sturrock 1994)

$$\nabla \times \mathbf{B} = \alpha \mathbf{B}. \tag{1}$$

Here α is a function of position (force-free parameter). The solutions of Equation (1) give potential fields (PFs) when $\alpha \equiv 0$, while they give linear force-free fields (LFFFs) when α is a non-zero constant. In the most general case where α changes spatially the solutions give nonlinear force-free fields (NLFFFs) (Woltjer 1958; Molodenskii 1969; Aly 1984; Berger 1985). Among these three kinds of force-free fields, PFs can give the minimum energy of a coronal magnetic structure. On the other hand, both LFFFs and NLFFFs contain free magnetic energy in the corona although LFFFs are obtained under a more restricted condition on α than NLFFFs, suggesting that LFFFs have difficulty in reconstructing a coronal magnetic structure full of variety formed on the Sun.

Reconstruction of a coronal magnetic structure using NLFFFs has well been studied, providing various practical methods such as the optimization method (Wheatland, Sturrock & Roumeliotis 2000; Wiegelmann 2004), magnetofrictional method (Yang, Sturrock & Antiochos 1986; McClymont & Mikic 1994; Roumeliotis 1996; McClymont, Jiao & Mikic 1997; Inoue et al. 2011), Grad-Rubin method (Grad & Rubin 1958; Amari et al. 1997; Amari, Boulmezaoud & Mikic 1999) and Green's function method (Yan & Sakurai 1997; 2000). A recent good review on these methods is found in Wiegelmann & Sakurai (2012).

An emerging flux region that produces active phenomena is initially formed through the emergence of intense magnetic flux below the solar surface, called *flux emergence*. One of the results from a flux-emergence magnetohydrodynamic (MHD) simulation suggests that the coronal magnetic structure of an emerging flux region is divided into inner quasi-static part and outer expanding (dynamic) part (Magara & Longcope 2003). A question then arises: how well a coronal magnetic structure formed via flux emergence is reconstructed using a force-free field; in other words how the force-free range of an emerging flux region develops.

When a magnetic field is force-free, the magnetic energy stored in a semi-infinite region above the solar surface is given by the following surface integral (e.g. Priest 1982):

$$E_{vr} = \frac{1}{4\pi} \int_{z=z_0} (xB_x + yB_y) B_z dxdy, \tag{2}$$

where x and y form a horizontal plane while z is directed upward ($z_0 = 0$ corresponds to the solar

surface, i.e. the photosphere). Equation (2) has widely been used to estimate the magnetic energy of a coronal structure from a photospheric magnetic field (Gary et al. 1987; Sakurai 1987; Klimchuk et al. 1992; Metcalf et al. 1995; McClymont et al. 1997; Wheatland & Metcalf 2006; Régnier & Priest 2007). In the present study we have performed a series of flux-emergence MHD simulations to reproduce several emerging flux regions with different magnetic configurations. We then calculate the magnetic energy of a coronal structure directly via the following volume integral:

$$E_m = \int_{z \geq z_0} \frac{B^2}{8\pi} dxdydz. \tag{3}$$

If a magnetic structure formed via flux emergence is in a force-free state, E_{vr} and E_m should be matched. In this respect, we have to mention the ambiguity of Equation (2), that is, the value of E_{vr} generally depends on the location of the origin of a Cartesian coordinate system when a magnetic field is not force-free (Wheatland & Metcalf 2006). Since a dynamically evolving magnetic structure reproduced by a flux-emergence simulation is not in a force-free state, it seems that Equation (2) cannot be applied to a flux-emergence simulation. To avoid this problem we have adjusted our simulations to remove the ambiguity of Equation (2), which is explained in detail in section 2. Accordingly we can use E_{vr} as a tool to investigate force-freeness of an emerging flux region.

The organization of this paper is as follows: In Section 2 we describe the setup of the simulations focused on force-freeness of an emerging flux region and explain how to avoid the ambiguity of Equation (2). Section 3 presents comparisons between E_{vr} and E_m of several emerging flux regions reproduced by the simulations. In Section 4 we discuss how the force-free range of an emerging flux region evolves and how it depends on the twist of a pre-emerged magnetic field. We also discuss the applicability of the virial theorem to an evolving magnetic structure formed via flux emergence on the Sun.

2. Setup of MHD simulations focused on force-freeness

We have performed a series of three-dimensional MHD simulations in a Cartesian coordinate system to reproduce several emerging flux regions with different magnetic configurations. The simulations have been done by solving ideal MHD equations given by

$$\frac{\partial \rho}{\partial t} + \nabla \cdot (\rho \mathbf{v}) = 0, \tag{4}$$

$$\rho \left[\frac{\partial \mathbf{v}}{\partial t} + (\mathbf{v} \cdot \nabla) \mathbf{v} \right] = -\nabla P + \frac{1}{4\pi} (\nabla \times \mathbf{B}) \times \mathbf{B} - \rho g_{\rm o} \hat{\mathbf{z}}, \tag{5}$$

$$\frac{\partial \mathbf{B}}{\partial t} = \nabla \times (\mathbf{v} \times \mathbf{B}), \tag{6}$$

$$\frac{\partial P}{\partial t} + \nabla \cdot (P\mathbf{v}) = -(\gamma - 1) P \nabla \cdot \mathbf{v}, \tag{7}$$

and

$$P = \frac{\rho \Re T}{\mu}, \tag{8}$$

where ρ, $\mathbf{v}$, $\mathbf{B}$, P, g_0, γ, μ, $\Re$, and T represent the gas density, fluid velocity, magnetic field, gas pressure, gravitational acceleration, adiabatic index ($\gamma = 5/3$ is assumed), mean molecular weight ($\mu = 0.6$ is assumed), gas constant and temperature, respectively. Table 1 shows the units of physical quantities used in the present study. The simulations have been performed within a domain $(-200, -200, -10) < (x, y, z) < (200, 200, 190)$ where the z-axis is directed upward and $z = 0$ corresponds to the solar surface. We adopt a non-uniform grid system $(\Delta x, \Delta y, \Delta z) = (0.1, 0.2, 0.1)$ for $(-8, -12, -10) < (x, y, z) < (8, 12, 15)$, while $\Delta x, \Delta y$ and Δz increase toward 4 as $|x|, |y|$ and z increase.

As an initial state, we place an isolated magnetic flux tube horizontally below the surface, whose axis is aligned with the y-axis, crossing the z-axis at $z = -4$. This flux tube is in mechanical equilibrium with a background atmosphere stratified under uniform gravity, which is the same as that in our previous works (An & Magara 2013; Lee & Magara 2014). The magnetic field composing a flux tube is characterized by a Gold-Hoyle profile, given by

$$\mathbf{B} = B_0 \frac{-b\, r\, \hat{\theta} + \hat{y}}{1 + b^2\, r^2}, \tag{9}$$

where $\hat{y}$ and $\hat{\theta}$ denote the axial and azimuthal directions of a flux tube, while r, B_0 and b represent the radial distance from the axis, the strength of a magnetic field at the axis and the twist parameter, respectively.

In the present study we investigate the evolution of five different flux tubes with the common background atmosphere (the photospheric pressure scale height is given by $H_{ph} = P_{ph}/(\rho_{ph} g_0)$). These flux tubes have the same radius ($r = 2$) and the same magnetic pressure at the interface with the background atmosphere (the gas pressure inside each flux tube is reduced to maintain pressure equilibrium at the interface) while they have different values of b and B_0: $b = 0.2$ (Extremely Weak Twist, EWT case), $b = 0.35$ (Weak Twist, WT case), $b = 0.5$ (Medium Twist, MT case), $b = 0.8$ (Strong Twist, ST case) and $b = 1.0$ (Extremely Strong Twist, EST case). More detailed information on these flux tubes is presented in Table 2. Figure 1 shows the distributions of gas pressure, magnetic pressure, gas density and temperature along the z-axis in all the cases.

To drive a simulation, we impose the following velocity perturbation to a flux tube during $0 < t < t_r$ in each case:

$$v_z = \begin{cases} \frac{v_0}{2} \cos\left(2\pi \frac{y}{\lambda}\right) \sin\left(\frac{\pi}{2} \frac{t}{t_r}\right) & \text{for } |y| \le \frac{\lambda}{2} \\ \frac{v_0}{2} \cos\left(2\pi \frac{y - \left[2L - \frac{\lambda}{2}\right] \frac{|y|}{y}}{4L - 2\lambda}\right) \sin\left(\frac{\pi}{2} \frac{t}{t_r}\right) & \text{for } |y| \ge \frac{\lambda}{2}. \end{cases} \tag{10}$$

where $t_r = 5$, $\lambda = 30$, $L = 200$ and $v_0 = 0.31$. This makes the axis of an emerging flux tube have a single Ω-shape on the Sun.

Boundary conditions are the same as the ones used in Magara (2012). A periodic boundary is placed at $y = \pm 200$, while an open boundary is placed at $x = \pm 200$ and $z = 190$. A fixed impermeable boundary is placed at $z = -10$. All these boundaries are accompanied by a wave damping zone, which avoids wave reflection at the boundaries. We enlarged a simulation domain compared to our previous

work (Magara 2012) and terminated all the simulations before the outermost part of an emerging magnetic field reaches the top and side boundaries, so an emerging field expands in a simulation domain as if it expanded in an unbounded space. This makes it justified to apply the virial theorem given by Eq. (2) to our simulations.

To avoid the ambiguity of Equation (2) mentioned in the previous section, we make ρ, P, v_z, B_x, B_y symmetric and v_x, v_y, B_z anti-symmetric with respect to 180-degree rotation about the z-axis so that a magnetic field and an electric current are always unidirectional (Magara & Longcope 2003). In this case,

$$B_x(x,y,z,t) = B_x(-x,-y,z,t), \tag{11}$$

$$B_y(x,y,z,t) = B_y(-x,-y,z,t), \tag{12}$$

and

$$B_z(x,y,z,t) = -B_z(-x,-y,z,t). \tag{13}$$

According to Wheatland & Metcalf (2006), the ambiguity of E_{vr} is caused by non-zero values of the horizontal components of the net Lorentz force:

$$F_x = -\frac{1}{4\pi}\int_{z=z_0} B_x B_z dxdy \tag{14}$$

and

$$F_y = -\frac{1}{4\pi}\int_{z=z_0} B_y B_z dxdy. \tag{15}$$

Since Equations (11)-(13) make both F_x and F_y vanish, E_{vr} gives a uniquely defined value in the present study.

3. Results

3.1. Overview of emerging flux regions

Firstly we present the overview of an emerging flux region in the EWT, WT, MT, ST and EST case. Figures 2a-2e show an emerging flux region obtained at a late phase in the EST (2a), ST (2b), MT (2c), WT (2d) and EWT (2e) case. In these figures, field lines are drawn in orange while isosurfaces of plasma β = 1.0 and 0.1 are given in red and blue, respectively. Figure 3 shows the time variation of the emerged flux rate (Magara 2012), showing how much the net axial magnetic flux emerges into the solar atmosphere in each case. This figure suggests that flux emergence seems to be saturated at a late phase in all the cases, although it is difficult to reproduce complete saturation because it takes a significant amount of computational time toward a late phase. We therefore select the final time step of a simulation in each case to show a late-phase emerging flux region in Figure 2.

According to Murray et al. (2006), the smaller the twist parameter is, the less emerged magnetic flux is, which suggests that a low plasma β region extends into the corona widely when the twist parameter is large. It is also found that a relatively high plasma β region is locally formed in the corona when the twist parameter is large (see the EST case in Figure 2).

3.2. *Comparisons between E_{vr} and E_m*

We then compare E_{vr} and E_m of an emerging flux region in these five cases. Figures 4a-c show how E_{vr} (dashed line) and E_m (solid line) change with time in the EST (black), ST (red), MT (green), WT (blue) and EWT (violet) cases, where E_{vr} and E_m are calculated by setting the bottom boundary at $z_0 = 0$ (4a), $z_0 = 1$ (4b) and $z_0 = 2$ (4c). From these figures, it is found that a difference between E_{vr} and E_m becomes small as z_0 increases, suggesting that a force-free approximation becomes reasonable when we use a magnetic field at a high atmospheric layer as a boundary condition. Another interesting result is that E_{vr} tends to be negative during an early phase of flux emergence, which is discussed in Section 4.

We further investigate the force-free range of an emerging flux region in a quantitative way. Figure 5 shows how the difference between E_{vr} and E_m changes with z_0 in the EST case, obtained at $t = 40$. Here we introduce the relative error between E_{vr} and E_m which is defined as

$$\Delta(z_0) = \frac{|E_m(z_0) - E_{vr}(z_0)|}{E_m(z_0)}. \tag{16}$$

In Figure 5 $\Delta(z_0)$ first decreases sharply toward a local minimum and then it gradually increases with z_0. This suggests that an emerging magnetic field becomes close to a force-free state as it goes up from the photosphere while it is then deviated from a force-free state in an upper atmosphere where an emerging field is in a dynamic state, continuously expanding outward. The conversion of the magnetic energy into the kinetic energy that produces the expansion of envelop magnetic flux becomes significant toward a late phase during which the injection of the magnetic energy into the atmosphere becomes weak. This causes a peak and the succeeding decrease of the magnetic energy shown in Figure 2.

The behavior of $\Delta(z_0)$ shown in Figure 5 is also found in the other cases once more than half of the net axial magnetic flux emerges into the photosphere. To determine the force-free range of an emerging flux region, we introduce a fitting function given by

$$f(z_0) = ae^{-hz_0} + be^{kz_0}, \tag{17}$$

where a, b, h and k are constant. $f(z_0)$ takes a global minimum at $z_0 = z_{min}$ given by

$$z_{min} = \frac{1}{k+h} \ln\left(\frac{ha}{kb}\right). \tag{18}$$

A fitting result of $f(z_0)$ is shown by a red curve in Figure 5. Using $f(z_0)$, we define a force-free range as z_l (lower limit) $\leq z_0 \leq z_u$ (upper limit) where z_0 satisfies $f(z_0) \leq f_c \equiv e^{-1}$. We confirmed that $f(z_{min})$ is always below f_c once more than half of the net axial magnetic flux emerges into the photosphere, which guarantees that we can determine a force-free range in all the cases. There is a tendency for z_l to become close to z_{min} as flux emergence proceeds.

Figures 6a and 6b show the time variations of z_l (6a) and z_u (6b) in the EST (black), ST (red), MT (green), WT (blue) and EWT (violet) case. $t = 0$ corresponds to the time when more than half of the net axial magnetic flux emerges into the photosphere. z_u tends to increase with time because

the expansion of envelop magnetic flux makes a force-free range extend upward, while z_l tends to decrease with time and then seems to be saturated because the expansion of magnetic flux toward a lower dense atmosphere is restricted. In general, as the twist parameter becomes large z_l becomes small whereas z_u becomes large, suggesting that an emerging flux region produced by a strongly twisted flux tube forms a wide force-free range.

Figure 7 shows the dependence of z_l (solid line), z_u (dashed line) and z_{min} (dotted line) on the twist parameter. The values of z_l, z_u and z_{min} are chosen at the final time step of a simulation in each case. It is found that as the twist parameter becomes large z_l decreases while z_u increases. Both z_l and z_u seems to be saturated in the weakly twisted cases (WT and EWT case).

4. Discussion

According to Figure 7, an emerging magnetic field becomes force-free at an atmospheric layer whose height is the order of H_{ph} (one H_{ph} for the EST case and $4H_{ph}$ for the WT and EWT cases). A similar result is also reported in observational works where the surface integral of magnetic pressure is compared with the surface integral of each component of the Lorentz force (Low 1984) in active regions (Metcalf et al. 1995; Moon et al. 2002). The so-called magnetic canopy (Gabriel 1976) also has this height (Steiner 2001). Figures 8a-c show how the ratio of the vertical component of the Lorentz force (F_z) to the magnetic pressure (F_0) changes with time as well as the location of the bottom boundary (z_0), both of which are given by

$$F_z = \frac{1}{8\pi}\int_{z=z_0}\left(B_z^2 - B_x^2 - B_y^2\right)dxdy, \tag{19}$$

and

$$F_0 = \frac{1}{8\pi}\int_{z=z_0}\left(B_x^2 + B_y^2 + B_z^2\right)dxdy. \tag{20}$$

If the ratio is much smaller than 1, then a magnetic field is close to a force-free state (Metcalf et al. 1995). Figures 8a-c suggests that an emerging magnetic field tends to be force-free at a high atmospheric layer during a late phase.

The twist of a flux tube makes an emerging magnetic field ‘rigid’; the magnetic tension force generated by a twisted field confines intense magnetic flux without the help of surrounding gas pressure, which means that a magnetic field is balanced by itself even in a high gas pressure region. This explains that an emerging magnetic field tends to be force-free at a low atmospheric layer with high gas pressure as the twist parameter increases.

Finally, let us discuss the behavior of E_{vr} of an evolving magnetic structure formed via flux emergence. This is related to how much flux emergence proceeds, that is to say, the emerged flux rate plays a key role in determining the sign of E_{vr}. To show this, we use a two-dimensional model illustrated in Figure 9a. In this model

$$E_{vr} \propto \int_{z=z_0} Q dx, \tag{21}$$

where $Q \equiv xB_xB_z$. The left and right panel in Figure 9a represents an early and late phase during which less than and more than half of the net axial magnetic flux emerges, respectively. A table given in lower part of each panel shows the signs of x, B_z, B_x and Q measured at the photosphere. These tables show that Q mostly takes a negative value before half of the net axial magnetic flux emerges into the photosphere while positive Q is found after more than half of the net axial magnetic flux emerges into the photosphere. Figure 9b shows a three-dimensional case obtained from one of the simulations (EST case). The photospheric distribution of $Q \equiv (xB_x + yB_y)B_z$ is given at the left panel ($t = 16$; before half of the net axial magnetic flux emerges) and right panel ($t = 32$; after half of the net axial magnetic flux emerges). Here we plot several selected field lines in white. In Figure 9b the violet areas where Q is negative are dominant during an early phase (left panel) while the red areas where Q is positive become significant during a late phase (right panel). The transition from the early phase to the late phase shown in Figure 3 is related to the transition of E_{vr} from decrease to increase found in Figure 4a. This result suggests that the virial theorem might be applied to a well-developed magnetic structure where flux emergence is almost saturated, although it may not be applied to a region where flux emergence actively proceeds.

The authors deeply appreciate useful comments by an anonymous referee. They also wish to thank the Kyung Hee University for general support of this work. KJH and TM give special thanks to Dr. Satoshi Inoue for his help. This work was financially supported by Basic Science Research Program (NRF-2013R1A1A2058705, PI: T. Magara) through the National Research Foundation of Korea (NRF) provided by the Ministry of Education, Science and Technology, as well as by the BK21 plus program through the NRF. Visualization in Figure 2 was done using VAPOR (Clyne et al. 2007).

References

Abbett, W. P., Mikić, Z., Linker, J. A., et al. 2004, Journal of Atmospheric and Solar-Terrestrial Physics, 66, 1257

Aly, J. J. 1984, ApJ, 283, 349

Amari, T., Aly, J. J., Luciani, J. F., Boulmezaoud, T. Z., & Mikic, Z. 1997, Sol. Phys., 174, 129

Amari, T., Boulmezaoud, T. Z., & Mikic, Z. 1999, A&A, 350, 1051

An, J. M., & Magara, T. 2013, ApJ, 773, 21

Berger, M. A. 1985, ApJS, 59, 433

Cameron, R., & Sammis, I. 1999, ApJL, 525, L61

Chen, P. F. 2011, Living Reviews in Solar Physics, 8, 1

Clyne, J., Mininni, P., Norton, A., & Rast, M. *New Journal of Physics*, 9, 301 (2007)

Forbes, T. G. 2000, J. Geophys. Res., 105, 23153,

Gabriel, A. H. 1976, Royal Society of London Philosophical Transactions Series A, 281, 339

Gary, G. A., Moore, R. L., Hagyard, M. J., & Haisch, B. M. 1987, ApJ, 314, 782

Grad H and Rubin H 1958 *2nd U.N. Conference on the Peaceful uses of Atomic Energy* vol 31 (Geneva) pp 190–197

Inoue, S., Kusano, K., Magara, T., Shiota, D., & Yamamoto, T. T. 2011, ApJ, 738, 161

Klimchuk, J. A., Canfield, R. C., & Rhoads, J. E. 1992, ApJ, 385, 327

Lee, H., & Magara, T. 2014, PASJ, 66, 42

Low, B. C. 1984, ApJ, 286, 772

Magara, T., & Longcope, D. W. 2003, ApJ, 586, 630

Magara, T. 2012, ApJ, 748, 53

McClymont, A. N., & Mikic, Z. 1994, ApJ, 422, 899

McClymont, A. N., Jiao, L., & Mikic, Z. 1997, Sol. Phys., 174, 191

Metcalf, T. R., Jiao, L., McClymont, A. N., Canfield, R. C., & Uitenbroek, H. 1995, ApJ, 439, 474

Molodenskii, M. M. 1969, Soviet Ast., 12, 585

Moon, Y.-J., Choe, G. S., Yun, H. S., Park, Y. D., & Mickey, D. L. 2002, ApJ, 568, 422

Murray, M. J., Hood, A. W., Moreno-Insertis, F., Galsgaard, K., & Archontis, V. 2006, A&A, 460, 909

Régnier, S., & Amari, T. 2004, A&A, 425, 345

Régnier, S., & Priest, E. R. 2007, ApJL, 669, L53

Roumeliotis, G. 1996, Bulletin of the American Astronomical Society, 28, 956

Sakurai, T. 1987, Sol. Phys., 113, 137

Shibata, K., & Magara, T. 2011, Living Reviews in Solar Physics, 8, 6

Steiner, O., & Murdin, P. 2000, Encyclopedia of Astronomy and Astrophysics,

Sturrock, P. A. 1994, Plasma Physics, An Introduction to the Theory of Astrophysical, Geophysical and Laboratory Plasmas, ISBN 0521448107, Cambridge University Press, 1994.,

Wang, H., Ewell, M. W., Jr., Zirin, H., & Ai, G. 1994, ApJ, 424, 436

Wang, H. 2006, ApJ, 649, 490

Wheatland, M. S., Sturrock, P. A., & Roumeliotis, G. 2000, ApJ, 540, 1150

Wheatland, M. S., & Metcalf, T. R. 2006, ApJ, 636, 1151

Wiegelmann, T. 2004, Sol. Phys., 219, 87

Wiegelmann, T., & Sakurai, T. 2012, Living Reviews in Solar Physics, 9, 5
Woltjer, L. 1958, Proceedings of the National Academy of Science, 44, 489
Yan, Y., & Sakurai, T. 1997, Sol. Phys., 174, 65
Yan, Y., & Sakurai, T. 2000, Sol. Phys., 195, 8
Yang, W. H., Sturrock, P. A., & Antiochos, S. K. 1986, ApJ, 309, 383

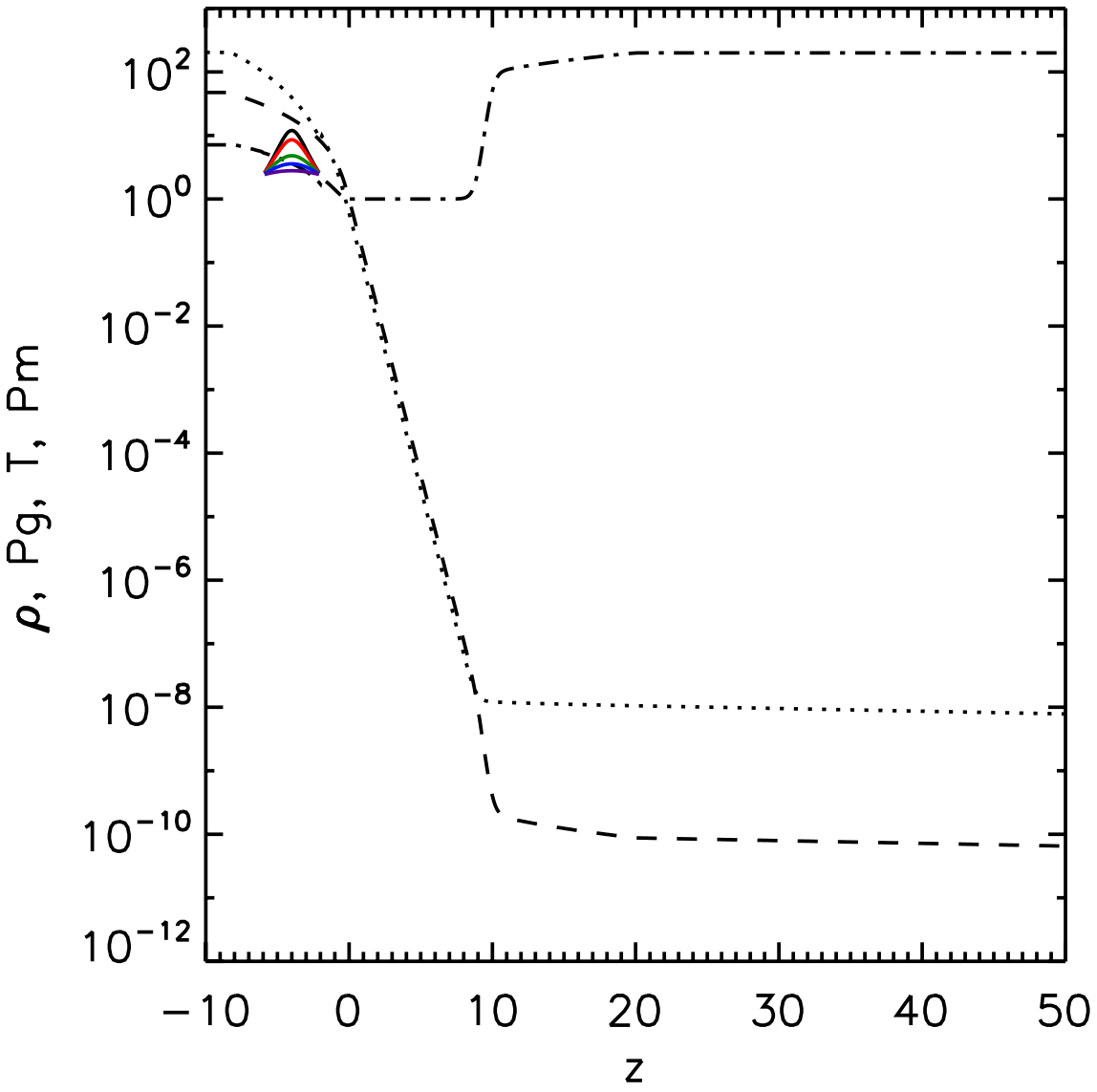

Fig. 1. Initial distributions of physical quantities along z-axis are presented in logarithmic scale. These quantities are gas pressure (dotted line), density (dashed line), temperature (dot-dashed line) and magnetic pressure (solid line). The magnetic pressure of EST, ST, MT, WT and EWT case is drawn in black, red, green, blue and violet, respectively. The background atmosphere is common for all the cases.

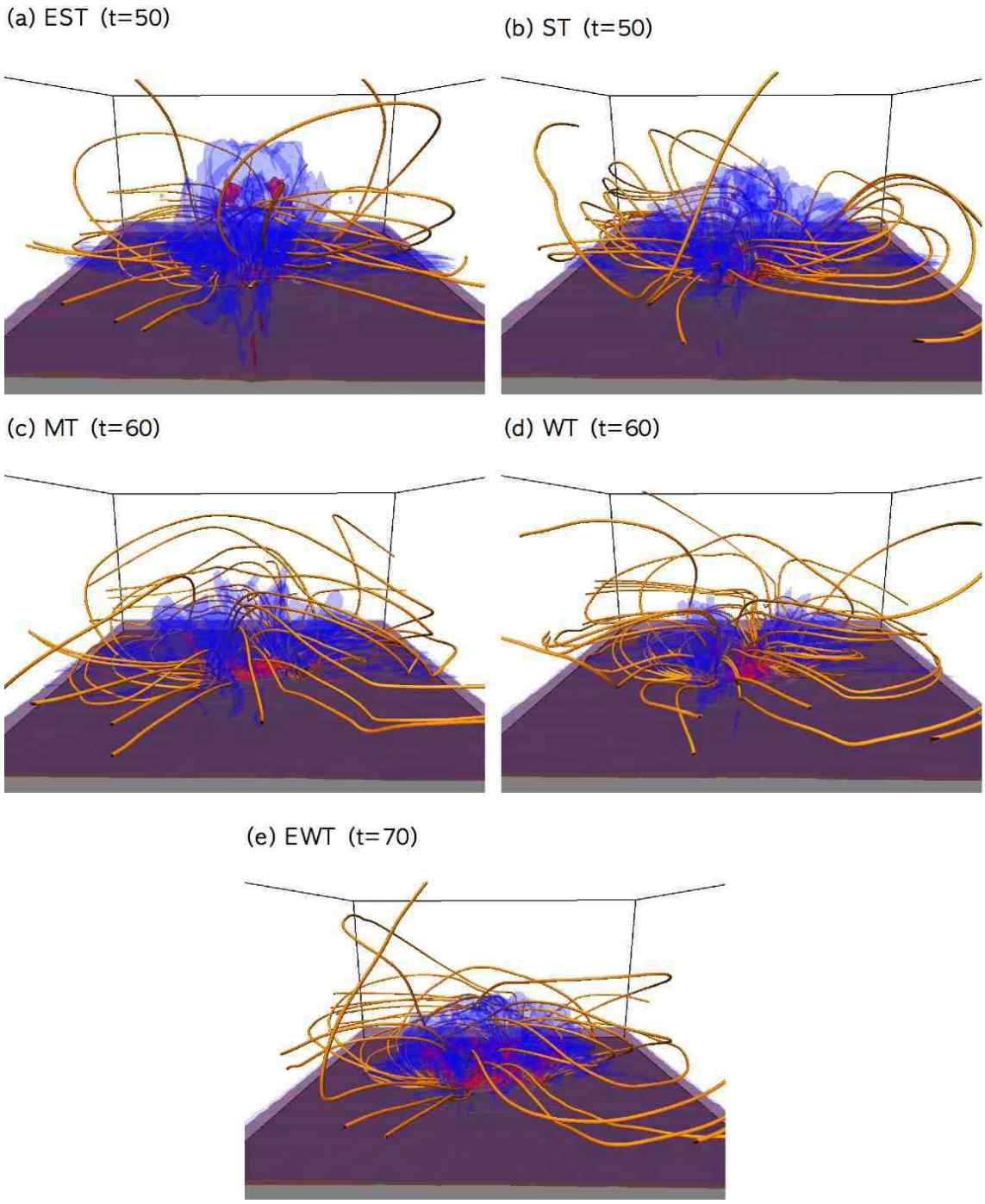

Fig. 2. Emerging flux region is presented in EST (2a), ST (2b), MT (2c), WT (2d) and EWT (2e) case. Field lines are drawn in orange while an isosurface of plasma β is given in red (plasma $\beta = 1$) and blue (plasma $\beta = 0.1$). The horizontal and vertical extents are $-80 \leq x, y \leq 80$ and $0 \leq z \leq 80$, respectively.

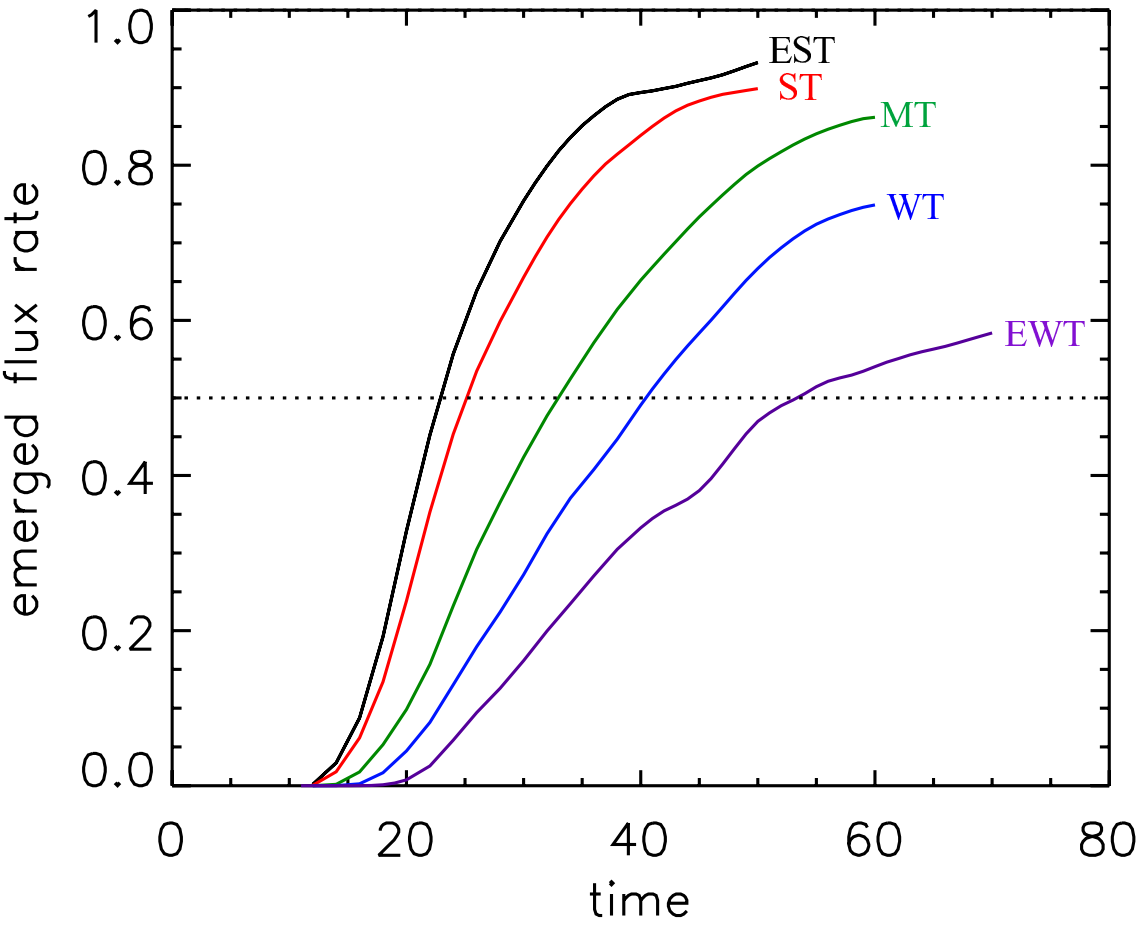

Fig. 3. Time variations of emerged flux rate in EST (black), ST (red), MT (green), WT (blue) and EWT (violet) case.

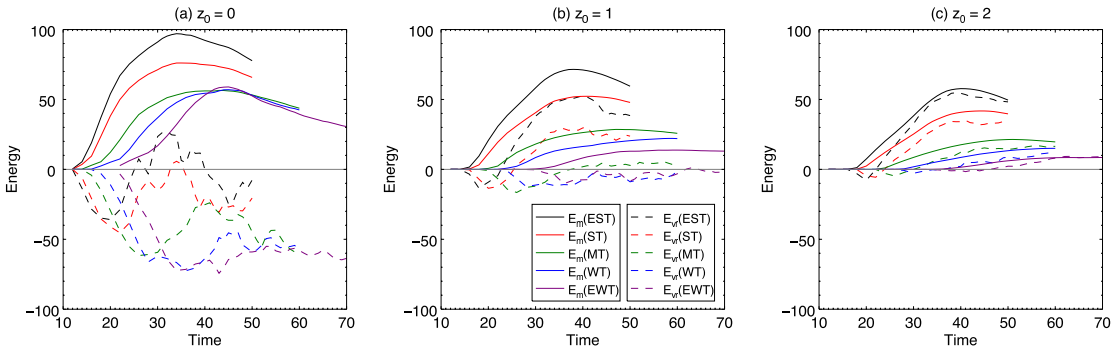

Fig. 4. Time variations of E_m (solid line) and E_{vr} (dashed line) are presented in EST (black), ST (red), MT (green), WT (blue) and EWT (violet) case. The bottom boundary used to calculate them is placed at $z_0 = 0$ (4a), 1 (4b) and 2 (4c).

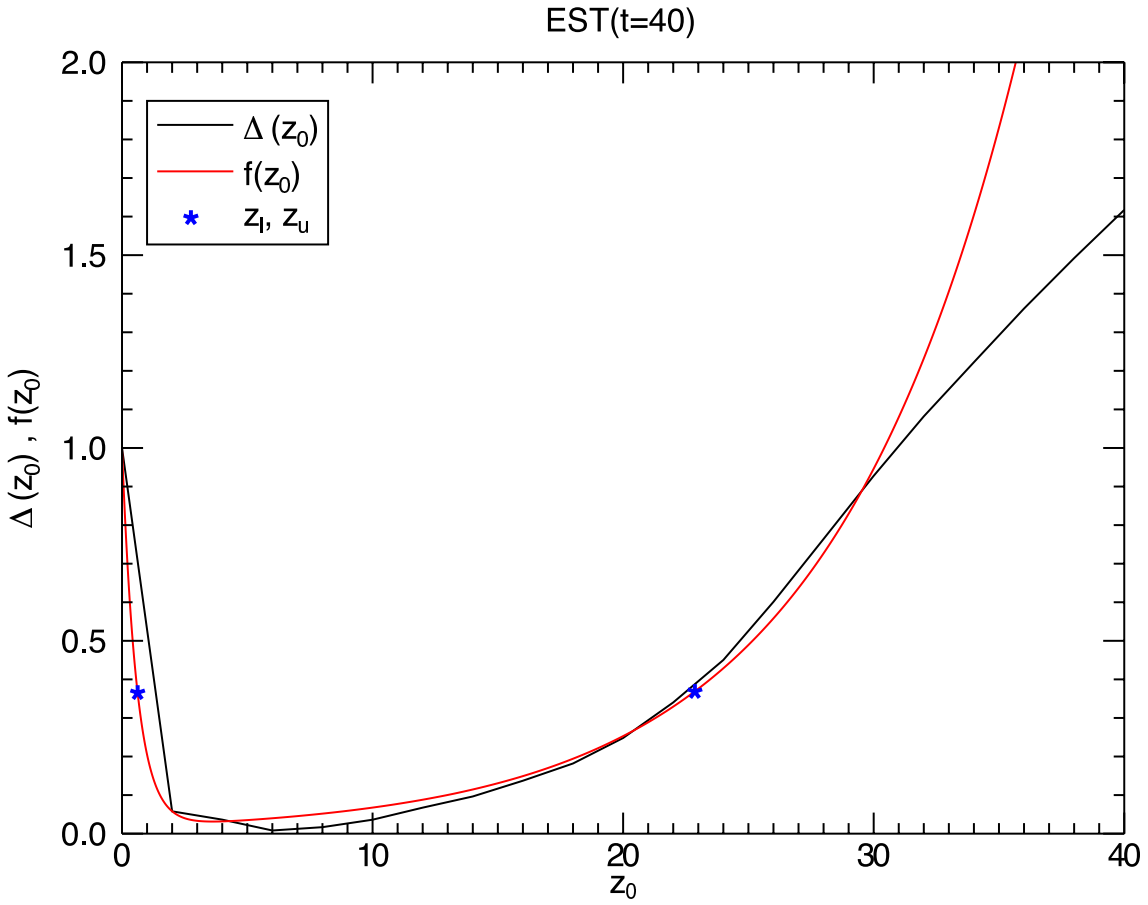

Fig. 5. The solid line represents $\Delta(z_0)$ given by Equation (16) in EST case ($t = 40$). A fitting curve given by Equation (17) is drawn in red. Two blue asterisks represent the locations of $z_0 = z_l$ and $z_0 = z_u$, respectively.

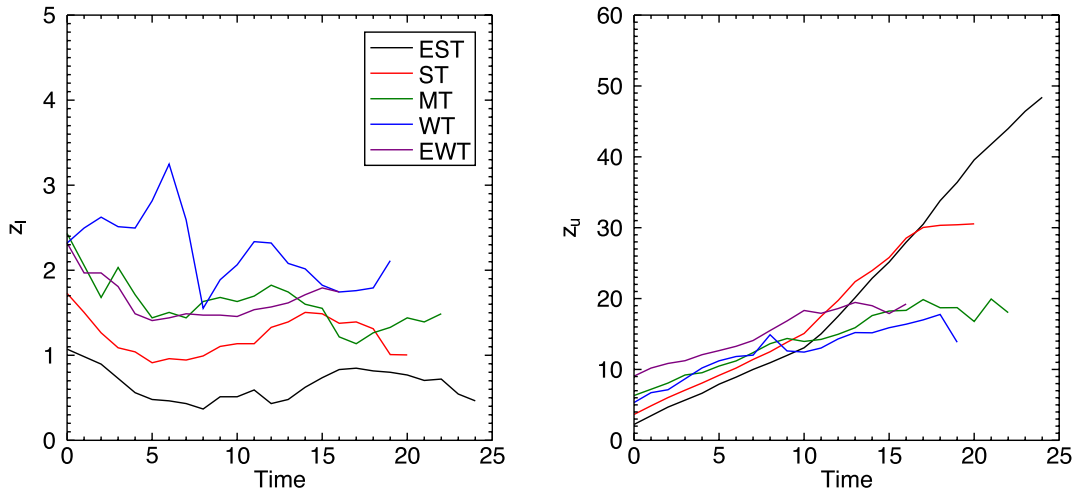

Fig. 6. Time variations of z_l (6a) and z_u (6b) are presented in EST (black), ST (red), MT (green), WT (blue) and EWT (violet) case. $t = 0$ corresponds to the time when more than half of the net axial magnetic flux emerges into the photosphere in each case.

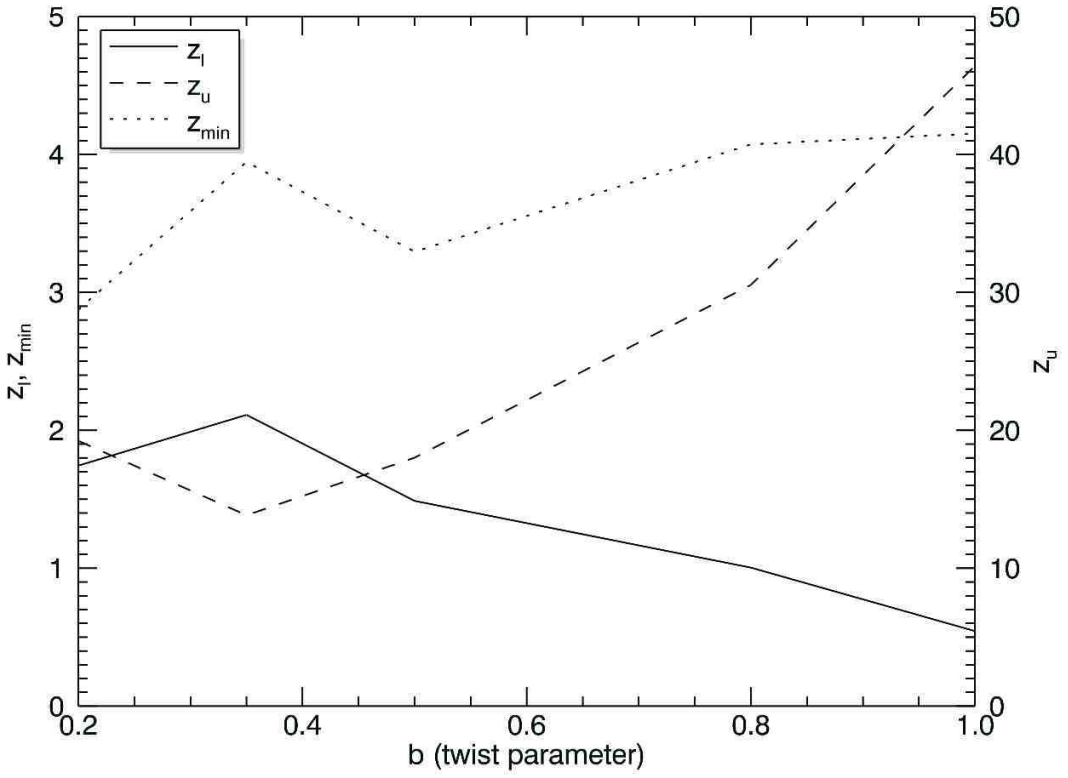

Fig. 7. Dependence of z_l (solid line, left vertical axis), z_u (dashed line, right vertical axis) and z_{min} (dotted line, left vertical axis) on twist parameter is presented in EWT ($b = 0.2$), WT ($b = 0.35$), MT ($b = 0.5$), ST ($b = 0.8$) and EST ($b = 1$) case. The values of z_l, z_u and z_{min} are chosen at the final time step of a simulation in each case.

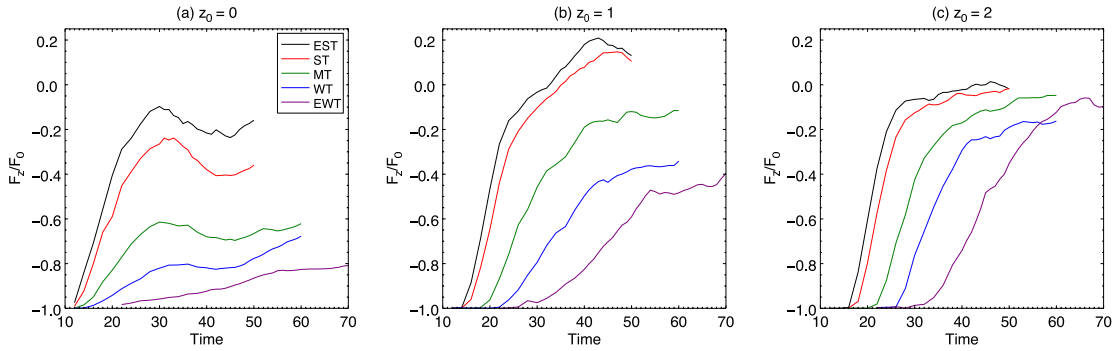

Fig. 8. Time variation of F_z/F_0 given by Equations (19) and (20) is presented in EST (black), ST (red), MT (green), WT (blue) and EWT (violet) case. The bottom boundary used to calculate F_z/F_0 is placed at $z_0 = 0$ (8a), 1 (8b) and 2 (8c).

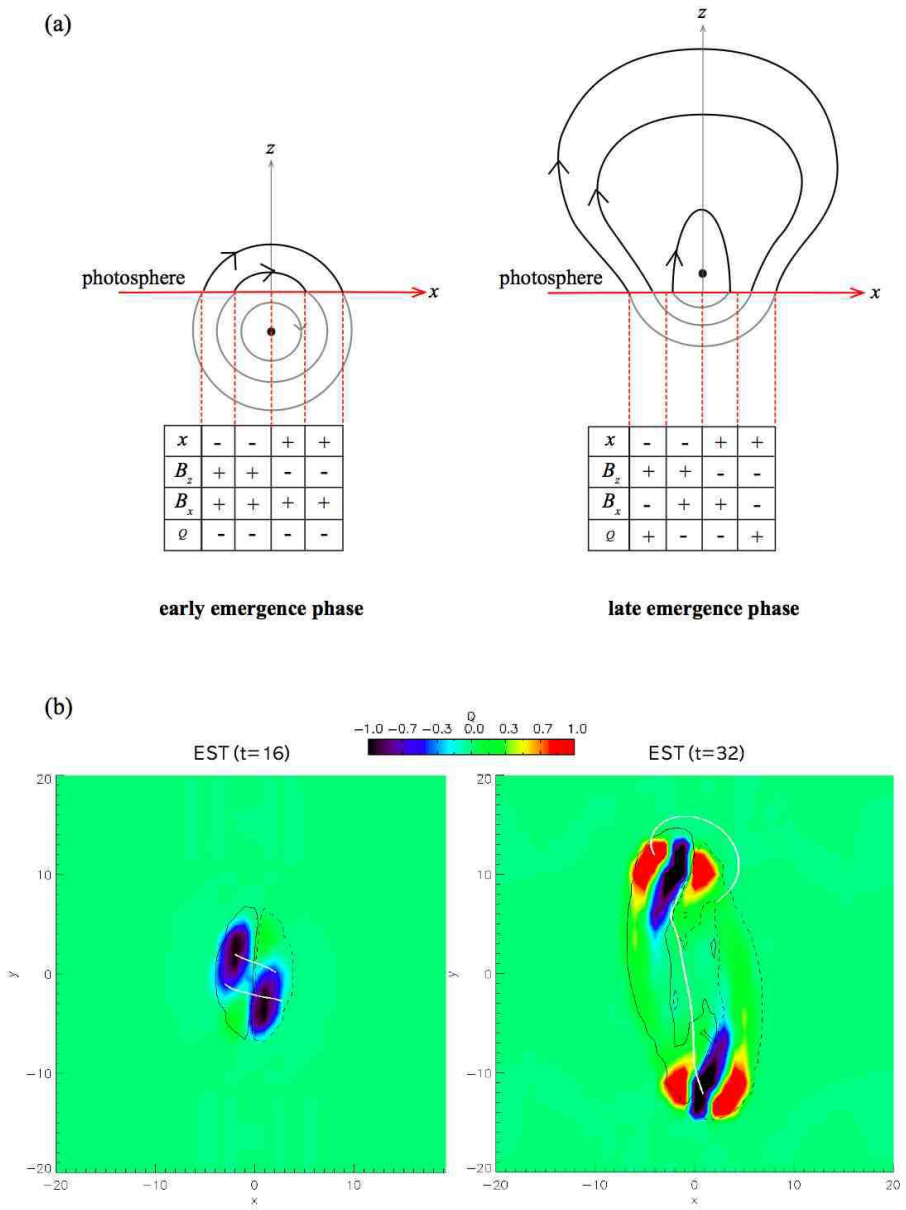

Fig. 9. (a) Distribution of $Q \equiv xB_xB_z$ during an early and late phase is schematically illustrated using a two-dimensional model. The left panel shows an early phase when less than half of the net axial magnetic flux emerges into the photosphere while the right panel shows a late phase when more than half of it emerges into the photosphere. The signs of x, B_z, B_x and Q are given at lower part of each panel. (b) Photospheric distribution of $Q \equiv (xB_x + yB_y)B_z$ is presented by a color map at the left panel (early phase) and right panel (late phase) in EST case . Contours indicate $B_z = 0.2$ (solid line) and -0.2 (dashed line). Several selected field lines are drawn in white.

Table 1. Units of Physical Quantities

Physical Quantity	$Unit$
Length	$2H_{ph}$ [a]
Velocity	$c_{s_{ph}}$ [b]
Time	$2H_{ph}$ / $c_{s_{ph}}$
Gas Density	ρ_{ph} [c]
Gas Pressure	$\rho_{ph}c^2_{s_{ph}}$
Temperature	T_{ph} [d]
Magnetic Field	$(\rho_{ph}c^2_{s_{ph}})^{1/2}$

[a] Photospheric gas pressure scale height.

[b] Photospheric adiabatic sound speed.

[c] Photospheric gas density.

[d] Photospheric temperature.

Table 2. Parameters used in the simulations

Case	r_f [a]	λ	l [b]	b	B_0	Φ_0 [c]
EST	2	30	6.3	1	17	88
ST	2	30	7.9	0.8	15	91
MT	2	30	13	0.5	11	96
WT	2	30	18	0.35	9.5	97
EWT	2	30	31	0.2	8.4	98

[a] Radius of a flux tube.

[b] $l \equiv 2\pi/b$, representing the axial distance of a field line that makes one helical turn around flux-tube axis.

[c] Net axial magnetic flux.